CSIAM Trans. Appl. Math.
doi: 10.4208/csiam-am.SO-2023-0037

Vol. **x**, No. x, pp. 1-26
xx 2024

DeepSPIM: Deep Semi-Proximal Iterative Method for Sparse-View CT Reconstruction with Convergence Guarantee

Deliang Wei[1], Fang Li[2,3,*], Xiao Shen[1] and Tieyong Zeng[4]

[1] *School of Mathematical Sciences, East China Normal University, Shanghai 200241, China.*
[2] *School of Mathematical Sciences, Key Laboratory of MEA (Ministry of Education) & Shanghai Key Laboratory of PMMP, East China Normal University, Shanghai 200241, China.*
[3] *Chongqing Key Laboratory of Precision Optics, Chongqing Institute of East China Normal University, Chongqing 401120, China.*
[4] *Department of Mathematical Science, The Chinese University of Hong Kong, Shatin, Hong Kong SAR, China.*

Received 22 July 2023; Accepted 23 February 2024

Abstract. Computed tomography (CT) reconstruction with sparse-view projections is a challenging problem in medical imaging. The learning-based methods lack generalization ability and mathematical interpretability. Since the model-based iterative reconstruction (IR) methods need inner gradient-based iterations to deal with the CT system matrix, the algorithms may not be efficient enough, and IR methods with deep networks have no convergence guarantees. In this paper, we propose an efficient deep semi-proximal iterative method (DeepSPIM) to reconstruct CT images from sparse-view projections. Unlike the existing IR methods, a carefully designed semi-proximal term is introduced to make the system matrix-related subproblem solvable. Theoretically, we give some useful mathematical analysis, including the existence of the solutions to the reconstruction model with an implicit image prior, the global convergence of the proposed method under gradient step denoiser assumption. Experimental results show that DeepSPIM is efficient and outperforms the closely related state-of-the-art methods regarding quantitative image quality values, details preservation, and structure recovery.

AMS subject classifications: 94A08, 68U10

Key words: Computed tomography, sparse-view reconstruction, iterative method, semi-proximal term, global convergence.

*Corresponding author. *Email addresses:* 52215500006@stu.ecnu.edu.cn (D. Wei), fli@math.ecnu.edu.cn (F. Li), sssxiao8@foxmail.com (X. Shen), zeng@hkbu.edu.hk (T. Zeng)

1 Introduction

Over the past few decades, X-ray computed tomography (CT) has been one of the most important diagnostic imaging techniques. However, radiation exposure may cause genetic mutations and increase cancer risk [8]. Low-dose CT can significantly reduce the threat of X-ray radiation. Sparse-view CT is a major strategy that only utilizes a few projected views for image reconstruction [10,39,40]. Unfortunately, the sparse-view CT strategy can also compromise image quality [6]. As a result, numerous exciting and practical models and algorithms have been proposed. In this paper, we focus on the semi-proximal iterative method for sparse-view CT reconstruction.

The following linear system can express the forward model for CT imaging:

$$f = Ru + \xi, \tag{1.1}$$

where $f \in \mathbb{R}^m$ is a vectorized projected data, $u \in \mathbb{R}^n$ is a vectorized 2D image, $R \in \mathbb{R}^{m\times n}$ is the projection matrix, and ξ is the Gaussian white noise added to the projected data. Due to the ill-posedness of the sparse-view CT image reconstruction problem, it is challenging to reconstruct u from f in practice. The most widely used method is the filtered back-projection (FBP) algorithm proposed by Kak and Slaney [28]. FBP is an efficient and robust direct reconstruction method. However, when the projection views are limited and polluted, FBP suffers from streaking artifacts. To address this issue, various methods have been proposed.

The first category is iterative reconstruction (IR) methods. Gordon *et al.* [19] presented the first IR method, the algebraic reconstruction technique (ART) to reconstruct CT images iteratively from no more than 60 views. Andersen and Kak [2] improved ART by applying the error correction terms simultaneously and presented the simultaneous algebraic reconstruction technique (SART). Shepp and Vardi [15] proposed the expectation maximization (EM) method to maximize the probability of the potential signal given the projected data. Though these methods are computationally efficient, it is difficult to provide satisfactory results when the projection views are highly sparse without image priors. In order to characterize the image features, Sidky *et al.* [39] applied the total variation (TV) prior to the few views and limited-angle data in divergent-beam CT. Sidky and Pan [40] have also studied the constrained TV minimization method for cone-beam CT. In order to design an efficient algorithmic for total variation based image restoration, Chen *et al.* [12] proposed a primal-dual fixed point algorithm for CT reconstruction. Kim *et al.* [31] improved the reconstruction effects by non-local TV prior. Xu *et al.* [51] introduced the dictionary-learning-based method to low-dose CT reconstruction. An improved tensor dictionary learning method is proposed by Wu *et al.* [48] for low-dose spectral CT reconstruction. IR methods with learning-based priors have also been studied. As an important method in compressed sensing, the convolutional sparse coding prior with gradient regularization (CSCGR) has been presented by Bao *et al.* [3] for sparse-view CT reconstruction. By directly working on the whole image, CSCGR can maintain

more details compared with dictionary-learning-based methods. In order to achieve better reconstruction results, deep-learning-based prior has been utilized in iterative methods using a plug-and-play (PnP) strategy. He *et al.* [22] proposed the parameterized plug-and-play ADMM (3pADMM) to reconstruct CT images with automatically selected parameters. Gupta *et al.* [20] proposed the relaxed projected gradient descent method (RPGD). They proved the convergence of RPGD under the non-expansive denoiser assumption. Wu *et al.* [47] proposed the dual-domain residual-based optimization network (DRONE) and solved the sparse-view reconstruction problem iteratively. He *et al.* [24] utilized deep frequency-recurrent prior (DFRP), and incorporated it into classical iterative reconstruction by proximal gradient descent. These reasonable priors, including TV and its extensions, low-rank sparsity, dictionary learning, convolutional sparse coding, and auto-encoding priors, can significantly improve imaging quality. However, there is no convergence guarantee for IR methods with deep image priors. Besides, the high computational cost hinders the application of IR methods since they often need hundreds of iterations to achieve a satisfactory result.

The second category is the deep-learning-based methods. Due to the great success of convolutional neural networks (CNNs) in image processing, some networks have been proposed for CT reconstruction. Inspired by the iterative shrinkage thresholding algorithm (ISTA) [5] for compressed sensing, Jin *et al.* [27] proposed FBPConvNet, a novel deep unfolding CNN-based algorithm incorporated with normal-convolutional operators. In order to incorporate CNN with wavelet transformations, Kang *et al.* [29] proposed the directional wavelet-based deep CNN for X-ray CT reconstruction. Han and Ye [21] introduced framing U-Net via deep convolutional framelets to sparse-view CT reconstruction. A residual encoder-decoder convolutional neural network (RED-CNN) for low-dose CT was studied by Chen *et al.* [11]. By combining the DenseNet [25] and deconvolution layer [49], Zhang *et al.* [56] presented DD-Net. Zhang *et al.* [55] proposed a meta-inversion network (MetaInv-Net) to tackle sparse view CT reconstruction. These methods take the result by FBP as an input, ignoring the data consistency in the sinogram domain. In order to address this issue, Boghiu *et al.* [13] proposed WNet, a data-driven dual-domain denoising model. WNet contains two encoder-decoder networks to perform denoising in the sinogram and reconstruction domain simultaneously. Experiments showed the superiority of WNet compared with other state-of-the-art baselines.

However, the methods mentioned above have some drawbacks. FBP suffers from limited and polluted projection data. IR methods like ART, SART, and EM are efficient, but the reconstructed images are not satisfactory. IR methods with learned priors can provide better reconstruction results, but they often need many iterations to converge numerically and have no theoretical convergence guarantees, such as CSCGR, DRONE, and DFRP. Deep-learning-based methods are efficient, and the reconstruction results are competitive. However, these methods lack generalization ability: When the testing images differ from the training images, the reconstruction results may not be satisfactory.

Therefore, in this paper, we propose DeepSPIM, a deep semi-proximal iterative method for sparse-view CT reconstruction with convergence guarantee. Compared with

the alternating direction method of multipliers (ADMM) [7], the proposed method has a semi-proximal term to make the CT reconstruction problem solvable. Moreover, we use the PnP framework to incorporate a pretrained deep prior to solve the denoising like subproblem. Overall, our main contributions are threefold:

- A semi-proximal iterative method with deep prior for sparse-view CT reconstruction is proposed.
- The global convergence result of our algorithm is established under mild assumptions.
- The proposed method can better recover the fine structures and details in CT images compared with some state-of-the-art methods.

The rest of this paper is organized as follows. In Section 2 we give the proposed method and some useful mathematical analysis. In Section 3, we present some experimental results. Finally, we conclude the paper in Section 4.

2 Method

This section will briefly review the typical CT reconstruction model with image priors first. Then, some existing state-of-the-art IR methods will be discussed. In these discussions, we will focus on the handling of the subproblem related to the system matrix R. Next, we will present DeepSPIM, an efficient IR algorithm for sparse-view CT reconstruction via a semi-proximal ADMM-based PnP framework. Finally, some useful mathematical properties including the global convergence result for the proposed method will be given.

2.1 CT reconstruction model

A typical sparse-view CT reconstruction model with prior F has the form

$$\min_u F(u)+\frac{\lambda}{2}\|f-Ru\|^2, \tag{2.1}$$

where $\|\cdot\|$ denotes the 2-norm for vectors or the Frobenius norm for matrices. $\lambda>0$ is a balancing parameter between the regularization prior term $F(\cdot)$, and the data fidelity term $\|f-Ru\|^2$.

Many convex optimization methods can be applied to solve (2.1) [5,7,14,16,18,35,45]. If we take the ADMM algorithm for example, by substituting u in (2.1) with variable v, the iterations are

$$\begin{aligned} &u^{k+1}=\arg\min_u F(u)+\frac{\beta}{2}\|u-v^k+b^k\|^2,\\ &(\lambda R^{\mathrm{T}}R+\beta I)v^{k+1}=\beta(u^{k+1}+b^k)+\lambda R^{\mathrm{T}}f,\\ &b^{k+1}=b^k+u^{k+1}-v^{k+1}, \end{aligned} \tag{2.2}$$

where I denotes the identity matrix with size $n\times n, b^k$ corresponds to the multiplier, and $\beta>0$ is the penalty parameter.

A straightforward way to solve the v-subproblem is to compute the inverse of the matrix $\lambda R^{\mathrm{T}}R+\beta I$. However, this could be time-consuming, because R is an ill-posed matrix, and has a large size in the sparse-view CT reconstruction problems. Alternatively, one can apply the conjugate gradient method, or the separable paraboloid surrogate method (SPSM) [18], see [3, 30, 52]. However, such methods are iterative, which often introduce additional CPU time. For instance, in CSCGR and DFRP, each outer iteration has 20 SPSM inner iterations. To address this issue, in [47], DRONE approximates $R^{\mathrm{T}}R$ by $\|R\|^2 I$. But when the projection views are extremely sparse, the approximation is inaccurate. In [55], the v-subproblem is parameterized by a neural network. However, this network needs to be trained carefully, which makes the reconstruction model complex. Therefore, in this paper, we aim to solve the v-subproblem efficiently by a semi-proximal ADMM method.

2.2 The proposed semi-proximal method

In this subsection, we will derive an effective IR algorithm for sparse-view CT reconstruction via a semi-proximal ADMM based PnP framework.

In order to make the v-subproblem solvable, we substitute Ru with v, and the Lagrangian function becomes

$$L_\beta(u,v,b)=F(u)+\frac{\lambda}{2}\|f-v\|^2+\beta\langle b,Ru-v\rangle+\frac{\beta}{2}\|Ru-v\|^2 \tag{2.3}$$

with the feasible set $\Omega_f=\{(u,v)\in\mathbb{R}^n\times\mathbb{R}^m: Ru-v=0\}$. Then the iterations by ADMM are

$$\begin{aligned} u^{k+1}&=\arg\min_u F(u)+\frac{\beta}{2}\|Ru-v^k+b^k\|^2,\\ v^{k+1}&=\arg\min_v \frac{\lambda}{2}\|f-v\|^2+\frac{\beta}{2}\|Ru^{k+1}-v+b^k\|^2,\\ b^{k+1}&=b^k+Ru^{k+1}-v^{k+1}. \end{aligned} \tag{2.4}$$

Now one can easily see that the v-subproblem is solvable. However, the u-subproblem is another sparse-view CT reconstruction problem with input v^k-b^k and penalty parameter β, which has a similar solve difficulty as the problem (2.1). To address this issue, we add a carefully designed semi-proximal term to the objective function in the u-subproblem and solve it by the proximal point algorithm (PPA) [34]. That is

$$u^{k+1}=\arg\min_u F(u)+\frac{\beta}{2}\|Ru-v^k+b^k\|^2+\frac{1}{2}\|u-u^k\|_P^2, \tag{2.5}$$

where P is a semi-definite positive matrix, and $\|\cdot\|_P$ is the induced semi matrix norm defined by $\|x\|_P=\sqrt{\langle x,Px\rangle}$.

The goal is to choose a specific positive semi-definite matrix P, such that (2.5) is equivalent to a Gaussian denoising task. Then the deep-learning-based Gaussian denoisers can be plugged into the algorithm. A tricky choice is $P=\alpha I-\beta R^{\mathrm{T}}R$. By choosing

$\alpha,\beta>0,\alpha\geq\beta\|R\|^2,P\succeq 0$ is a positive semi-definite matrix by the following Lemma 2.1. Note that similar results as Lemma 2.1 has been used in many generalized proximal point algorithms.

Lemma 2.1. *Let R be any matrix of size $m\times n$, and R^{T} be the adjoint/transpose matrix of R. Let $\alpha\geq\beta\|R\|^2,\alpha,\beta>0$. Then $P=\alpha I-\beta R^{\mathrm{T}}R$ is a positive semi-definite matrix. Moreover, the problem* (2.5) *is equivalent to the following problem:*

$$u^{k+1}=\arg\min_u F(u)+\frac{\alpha}{2}\|u-u^k+w^k\|^2, \tag{2.6}$$

where $w^k=(\beta/\alpha)R^{\mathrm{T}}(Ru^k-v^k+b^k)$.

The proof of Lemma 2.1 is given in Appendix A.1. By Lemma 2.1, the problem (2.5) is equivalent to problem (2.6), which is a typical Gaussian noise removal task with input u^k-w^k. We replace this step in the ADMM algorithm with an arbitrary Gaussian denoiser in a plug-and-play fashion

$$\begin{aligned}
u^{k+1}&=D_\alpha\left(u^k-\frac{\beta}{\alpha}R^{\mathrm{T}}(Ru^k-v^k+b^k)\right),\\
v^{k+1}&=\frac{\lambda f+\beta Ru^{k+1}+\beta b^k}{\lambda+\beta},\\
b^{k+1}&=b^k+Ru^{k+1}-v^{k+1},
\end{aligned} \tag{2.7}$$

where D_α is a Gaussian denoiser with denoise strength α. When α gets bigger, the denoise strength gets smaller. In this paper, we choose DnCNN [54], a simple yet powerful Gaussian denoiser based on residual learning [23] as D_α. The method in (2.7) is dubbed DeepSPIM, and is summarized in Algorithm 1. The architecture of DeepSPIM is illustrated in Fig. 1. As shown in Fig. 1, DeepSPIM optimizes the CT image u and the projected Radon data v alternatively to reach the final reconstruction.

Algorithm 1. DeepSPIM for Sparse-View CT Reconstruction.

1: **Given** $\alpha,\beta,\lambda>0,f\in\mathbb{R}^m$, and Gaussian denoiser D_α.
2: **Initialize** $k=0,u^0,v^0,b^0$.
3: **Repeat**
4: $u^{k+1}=D_\alpha\left(u^k-\frac{\beta}{\alpha}R^{\mathrm{T}}(Ru^k-v^k+b^k)\right)$.
5: $v^{k+1}=\frac{\lambda f+\beta Ru^{k+1}+\beta b^k}{\lambda+\beta}$.
6: $b^{k+1}=b^k+Ru^{k+1}-v^{k+1}$.
7: $k=k+1$.
8: **Until** u^{k+1} satisfies the stopping criteria, return u^{k+1} and stop.

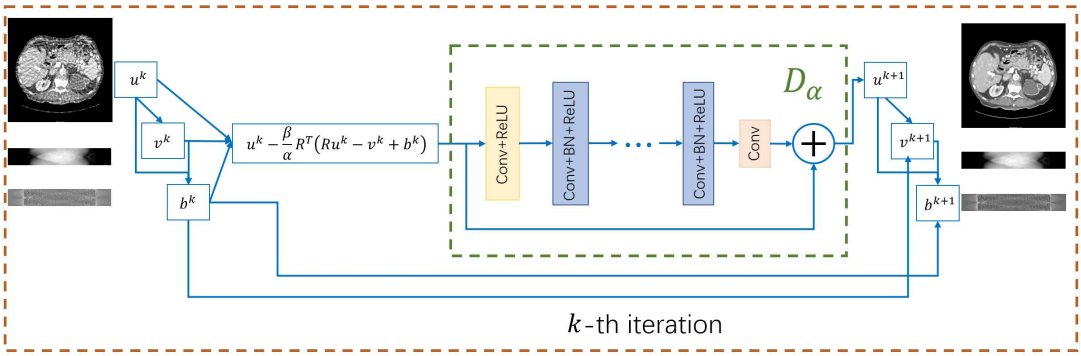

Figure 1: Algorithm framework for DeepSPIM at k-th iteration.

2.3 Assumptions on the Gaussian denoiser D

In order to analyze the model (2.1) and the proposed method (2.7), we need to make some mild assumptions on the regularization term $F(\cdot)$ and the Gaussian denoiser D. Since in experiments we train the denoiser D_α with L^2 loss function, D_α is a good approximation of minimum mean square error (MMSE) estimator $\hat{D}_\alpha(y)=\mathrm{E}[x|y]$. By Tweedie's formula, $\hat{D}_\alpha = I+\alpha^2\nabla\log p(\cdot)$, where I is the identity operator and $p(\cdot)$ denotes a smoothed probability density of images [17]. Therefore, we assume D is the form of the gradient step (GS) denoisers as introduced in [26].

Assumption 2.1. The Gaussian denoiser satisfies $D_\alpha = \nabla h_\alpha$, where

$$h_\alpha(x) = \frac{1}{2}\|x\|^2 - g_\alpha(x). \tag{2.8}$$

$g_\alpha : \mathbb{R}^n \to \mathbb{R}, g_\alpha \in C^2$ is a scalar function parameterized by a differentiable neural network, bounded from below, and ∇g_α is L-Lipschitz with $L<1$.

When g_α is a C^2 function, ∇g_α is L-Lipschitz with $L<1$, and it is proved [26] that

$$D_\alpha(z) = Prox_{\frac{F}{\alpha}}(z) = \arg\min_x F(x) + \frac{\alpha}{2}\|x-z\|^2 \tag{2.9}$$

with $F:\mathbb{R}^n \to \mathbb{R}\cup\{+\infty\}$ defined by

$$F(x) := \begin{cases} \alpha g_\alpha\left(D_\alpha^{-1}(x)\right) - \dfrac{\alpha}{2}\left\|D_\alpha^{-1}(x)-x\right\|^2, & \text{if} \quad x\in \mathrm{Im}(D_\alpha), \\ +\infty, & \text{otherwise.} \end{cases} \tag{2.10}$$

Despite F may be non-convex, D_α is one-to-one. Note that by (2.8) and $D_\alpha = \nabla h_\alpha$, we have

$$D_\alpha(x) = \nabla h_\alpha(x) = x - \nabla g_\alpha(x) = (I - \nabla g_\alpha)(x). \tag{2.11}$$

That is, when Assumption 2.1 is satisfied, the Gaussian denoiser D_α outputs the difference of the input image x and the predicted noise $\nabla g_\alpha(x)$. Therefore, the residual-learning-based Gaussian denoiser DnCNN as shown in Fig. 1 matches with Assumption 2.1, which demonstrates that Assumption 2.1 is a proper hypothesis for DeepSPIM.

Also note that, in Assumption 2.1, the residual $I-D_\beta$ is required to satisfy the L-Lipschitz condition with $L<1$. There have been some approaches to ensure this. In [36], the real spectral normalization (RealSN) technique was proposed to ensure $L<1$ for DnCNN. It was shown that RealSN is an effective training method without compromising the denoising performance. In [26], a regularization term $\|\nabla g_\alpha\|_*$ was added to the original loss function to ensure the Lipschitz condition. However, the method can only ensure the L-Lipschitz condition on the training set. Therefore, in this paper, we train the denoiser with RealSN.

2.4 Theoretical results for the proposed algorithm

In this subsection, we prove the global convergence of DeepSPIM. It should be noted that since PnP-ADMM was proposed [43], there has been many works on the convergence of PnP-ADMM, see [9,36,41]. However, to the best of our knowledge, no semi-proximal PnP method like DeepSPIM has been proposed. Therefore, we aim to prove the convergence of DeepSPIM under Assumption 2.1.

Theorem 2.1 gives the existence of solutions over $\mathbb{R}^n$ to the problem (2.1) under mild assumptions.

Theorem 2.1. *Let $\mathbb{F}=\mathbb{R}^m,\mathbb{E}=\mathbb{R}^n,f\in\mathbb{F}$ is a fixed vector and $\lambda>0$. Given any compact set $S\in\mathbb{E}$, there exists at least one minimizer $u^*\in\mathbb{E}$ for* (2.1) *over S if*

- *Assumption* 2.1 *is satisfied,*
- *$F:\mathbb{E}\to[-\infty,+\infty]$ is proper and closed,*
- *$S\cap dom(F)\neq\emptyset$.*

If we further assume that R has full column rank, then given any closed compact set $S\in\mathbb{E}$, there exists at least one minimizer $u^*\in\mathbb{E}$ for (2.1) *over S.*

The proof of Theorem 2.1 is given in Appendix A.2. Theorem 2.1 shows that given projected data $f\in\mathbb{R}^m$, there is at least one minimizer u^* over the closed set $S\subset\mathbb{R}^n$, such as $S=\mathbb{R}^n$ and $S=[0,255]^n$.

We prove that the Lagrangian function defined in (2.3) is non-increasing and the convergence of Algorithm 1.

Theorem 2.2. *Given $\alpha,\beta,\lambda,\sigma>0,f\in\mathbb{R}^m,R\in\mathbb{R}^{m\times n}$ be the system matrix. Let F be the regularization term defined in* (2.10)*, and $\{(u^k,v^k,b^k)\}_{k=0}^\infty$ be the sequence generated by DeepSPIM defined in* (2.7)*. If*

- *Assumption* 2.1 *is satisfied,*
- $\lambda \leq \frac{1+\sqrt{5}}{2}\beta$, $\alpha \geq \beta\|R\|^2$, $\alpha,\beta,\lambda > 0$,

then

- *the Lagrangian function* $L_\beta(u^k,v^k,b^k)$ *in* (2.3) *is lower bounded and non-increasing,*
- $\{(u^k,v^k,b^k)\}$ *is bounded,*
- (u^k,v^k,b^k) *converges weakly to* (u^*,v^*,b^*)*, a minimizer of* $L_\beta(u,v,b)$.

The proof of Theorem 2.2 is given in Appendix A.3. In Theorem 2.3, we establish the relationship between (u^*,v^*,b^*) and the original problem (2.1).

Theorem 2.3. *Let* $\{(u^k,v^k,b^k)\}_{k=0}^{\infty}$ *be the sequence generated by DeepSPIM, and* (u^*,v^*,b^*) *be the minimizer described in Theorem* 2.2*. When the minimizer of* (2.1) *and* (2.3) *is unique, under the same assumptions as Theorem* 2.2, (u^*,v^*,b^*) *satisfies that*

- $v^* = Ru^*$,
- u^* *is a minimizer of* (2.1).

The proof of Theorem 2.3 is given in Appendix A.4. By Theorem 2.3, the convergent solution u^* by the proposed method is indeed a minimizer of the original problem (2.1), which guarantees that u^* is the desired reconstructed CT image.

3 Experiments

In this section, we show some experimental results to illustrate the effectiveness and efficiency of our method. We use three typical CT images for detailed visual comparisons as displayed in Fig. 2, and a test data set containing ten typical images from "the NIH-AAPM-Mayo Clinic Low Dose CT Grand Challenge" [42] as shown in Fig. 3. The

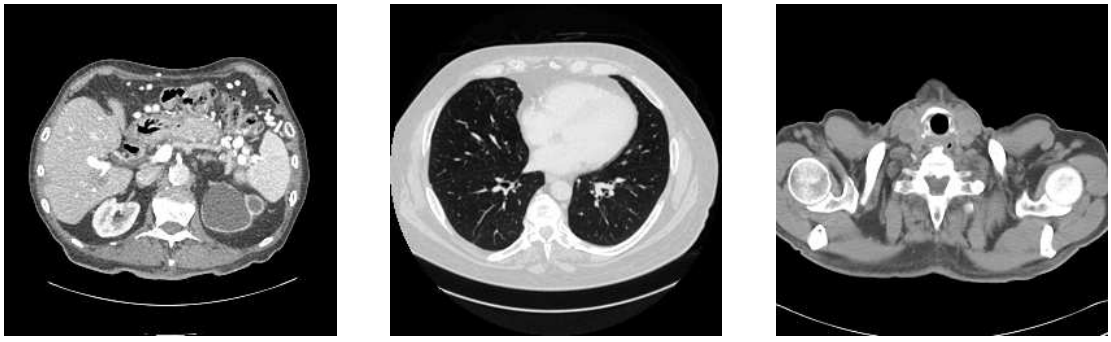

(a) Abdominal (b) Thoracic (c) Pelvic

Figure 2: Three test CT images.

projection data in parallel-beam geometry were simulated by Siddon's ray-driven algorithm [38], which can be implemented by the `radon` command in Matlab or `scikit` package in Python. For other projection settings, one can refer to [37]. The system matrix R is obtained consequently. We test three sparse-view settings: 30 views, 45 views, and 60 views. The projection views are sampled uniformly from 180 views. All the experiments are conducted under the Linux system, Python 3.8.12, Pytorch 1.10.2, and MATLAB R2021a. CPU Intel Intel(R) Xeon(R) CPU E5-2698 v4 @2.20GHz, GPU3090.

For the Gaussian denoiser D_α in Algorithm 1, we select DnCNN [54], a simple yet powerful Gaussian denoiser based on the residual learning [23]. We use $1/\alpha^2$ to represent the denoising strength of DnCNN as suggested in [9]. For example, when $\alpha=1/\sqrt{10}$, it means that the DnCNN denoiser is particularly trained to remove Gaussian noise with standard derivation 10.

Since the proposed method is a plug-and-play method, we use the 800 DIV2K natural images [1] as the training set. The images are divided into 96×96 patches. No obvious denoising improvement is observed with a larger patch size. Note that in the training procedures, no information about CT images is used. In order to ensure the Lipschitz condition in Assumption 2.1, we select $L=0.99$ and adopt RealSN in [36] in the training procedure. The network is trained using the ADAM optimizer for 50 epochs, with a mini-batch size of 64. The learning rate was 10^{-4} in the first 25 epochs, then decreased to 10^{-5}.

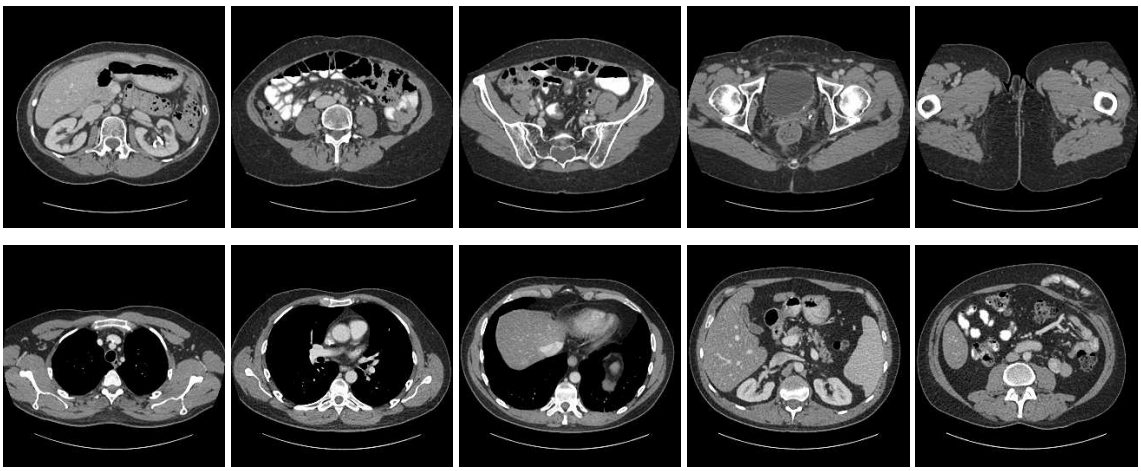

Figure 3: CT images named from "01" to "10" in the test dataset.

3.1 Parameter settings

The parameters are set as follows. For the denoising strength α, we need a smaller α when the projection view get fewer. Empirically, we choose $\alpha=1/\sqrt{8},1/\sqrt{8},1/\sqrt{10}$ when the projection view number is 60, 45, and 30 respectively. The augmented parameter β should be tuned in the range $(0,\alpha/\|R\|^2]$ according to Theorem 2.2. We empirically set

$\beta = \alpha / \|R\|^2$ in all experiments. Although Theorem 2.2 gives the sufficient conditions to ensure the convergence of Algorithm 1, experiments show that we do not need to restrict $\lambda \in (0, (1+\sqrt{5})\beta/2)$. Therefore, λ is tuned from $(0, +\infty)$ manually.

We set the stopping criteria in Algorithm 1 as the relative error $Err^k < 0.008$ or $k > 50$. The relative error is defined as

$$Err^k = \frac{\|u^k - u^{k-1}\|}{\|u^{k-1}\|}. \tag{3.1}$$

3.2 Reconstruction results

We compare our method with FBP [28], FBPConvNet by Jin *et al.* [27], CSCGR by Bao *et al.* [3], DFRP by He *et al.* [24], WNet by Boghiu *et al.* [13], and DRONE by Wu *et al.* [47]. All methods are fine-tuned to reach the best visual performance.

We show an overall result of PSNR values and SSIM values in Table 1. The highest value is marked in **boldface**. It can be seen that the PSNR values and SSIM values by DeepSPIM are higher than other methods in most cases. Moreover, our PSNR and SSIM values outperform the second-best method by 3.38dB and 0.0154 on average, respectively.

Table 1: The comparisons of PSNR values and SSIM values by different methods for sparse-view CT reconstruction on the three test images as shown in Fig. 2. The methods are FBP [28], FBPConvNet (FNet for short) [27], CSCGR [3], DFRP [24], WNet [13], DRONE [47], and the proposed DeepSPIM.

Images	Metrics	FBP	FNet	CSCGR	DFRP	WNet	DRONE	DeepSPIM
Abdominal	PSNR	26.76	33.50	34.86	34.34	36.23	35.72	**38.99**
30 views	SSIM	0.4677	0.8550	0.8960	0.8700	0.9150	0.9013	**0.9410**
Abdominal	PSNR	29.88	35.78	38.86	37.83	39.90	38.87	**41.96**
45 views	SSIM	0.6101	0.9006	0.9441	0.9269	0.9606	0.9465	**0.9640**
Abdominal	PSNR	32.18	37.51	41.65	40.77	40.71	40.91	**43.20**
60 views	SSIM	0.7133	0.9065	0.9660	0.9565	0.9560	0.9530	**0.9695**
Thoracic	PSNR	24.82	31.90	33.02	32.11	35.14	35.94	**39.16**
30 views	SSIM	0.4093	0.8305	0.8795	0.8369	0.9247	0.9306	**0.9565**
Thoracic	PSNR	28.01	34.72	37.11	37.97	38.98	38.55	**42.43**
45 views	SSIM	0.5445	0.9033	0.9391	0.9646	0.9447	0.9580	**0.9746**
Thoracic	PSNR	30.38	36.41	40.09	41.32	40.08	40.51	**44.06**
60 views	SSIM	0.6518	0.8896	0.9721	0.9722	0.9707	0.9720	**0.9802**
Pelvic	PSNR	26.71	31.87	35.40	36.39	39.55	39.69	**42.50**
30 views	SSIM	0.4681	0.8566	0.9054	0.9009	0.9663	0.9729	**0.9739**
Pelvic	PSNR	30.40	34.12	40.06	42.23	41.42	42.31	**45.61**
45 views	SSIM	0.6261	0.8617	0.9601	0.9707	0.9767	0.9790	**0.9848**
Pelvic	PSNR	32.78	36.88	43.25	47.09	42.98	43.34	**48.37**
60 views	SSIM	0.7379	0.9246	0.9781	0.9888	0.9832	0.9834	**0.9913**

In Fig. 4, we show the results of the image "Abdominal" from 60 projection views. We enlarge the green part. We can see that the results in Figs. 4(a)-4(b) by FBP and FBPConvNet are not satisfactory. Though CSCGR can retain the structures well, there are some noise residuals, see Fig. 4(c). The results in Figs. 4(d)-4(e) by DFRP and WNet are smooth, but seem to be blurred, and the edges are not clear. The result by DRONE has some staircase artifacts, see Fig. 4(f). Compared with these methods, ours can provide an artifact-free image with better structures, see Fig. 4(g). The residual images shown in Fig. 4 show that the image by DeepSPIM is closer to the potential image.

We also show the results when reconstructing the image "Thoracic" from 30 projection views in Fig. 5. In this very low-dose setting, it is difficult to recover the enlarged structure. In Fig. 5(a), the result by FBP illustrates the difficulty. In Fig. 5(b), FBPConvNet can recover the edge and most of the streaking artifacts, but failed to recover the structure. The results by CSCGR and DFRP, as shown in Figs. 5(c)-5(d), have some artifacts. WNet and DRONE can better recover the enlarged structures, but still blurred, see Figs. 5(e)-5(f). Compared with these methods, the image in Fig. 5(g) by DeepSPIM has clear edges and structures, with less streaking artifacts residuals. The residual images in Figs. 5(a)-5(g) also illustrate the effectiveness of the proposed method.

In order to further evaluate the performance of Algorithm 1 for sparse-view CT reconstruction, tests are performed on a test data set containing ten typical CT images. Quantitative results on this test set are listed in Table 2. We can notice that the PSNR values and SSIM values by DeepSPIM are higher than other methods. In terms of PSNR, the average gain of our method over the second-best method is about 1.71 dB, which shows the potential ability of DeepSPIM on data sets.

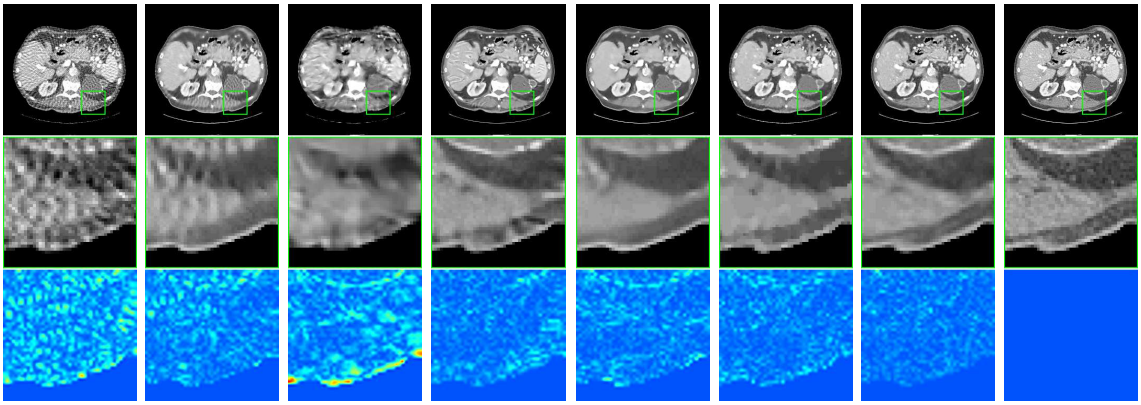

(a) FBP (b) FBPConvNet (c) CSCGR (d) DFRP (e) WNet (f) DRONE (g) DeepSPIM (h) Ground truth

Figure 4: Results of different methods when reconstructing the image "Abdominal" from 60 views. The second row is the enlarged part of the first row. The third row is the difference between the reconstructed image u and the ground truth image I. (a) Result by FBP, PSNR=32.18 dB. (b) Result by FBPConvNet, PSNR=37.51 dB. (c) Result by CSCGR, PSNR=41.65 dB. (d) Result by DFRP, PSNR=40.77 dB. (e) Result by WNet, PSNR=40.71 dB. (f) Result by DRONE, PSNR=40.91 dB. (g) Result by DeepSPIM, PSNR=43.20 dB. (h) Ground truth.

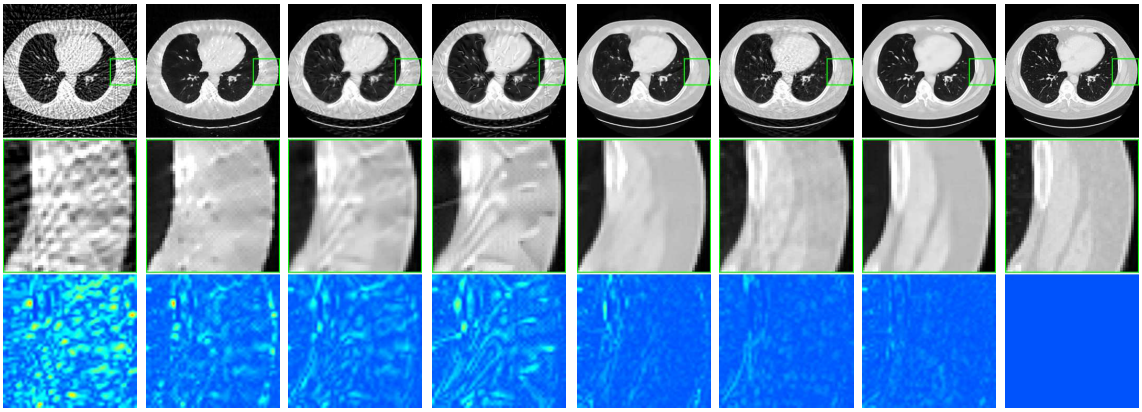

(a) FBP (b) FBPConvNet (c) CSCGR (d) DFRP (e) WNet (f) DRONE (g) DeepSPIM (h) Ground truth

Figure 5: Results of different methods when reconstructing the image "Thoracic" from 30 views. The second row is the enlarged part in the first row. The third row is the difference between the reconstructed image u and the ground truth image I. (a) Result by FBP, PSNR=24.82 dB. (b) Result by FBPConvNet, PSNR=31.90dB. (c) Result by CSCGR, PSNR=33.02dB. (d) Result by DFRP, PSNR=32.11dB. (e) Result by WNet, PSNR=35.14dB. (f) Result by DRONE, PSNR=35.94dB. (g) Result by DeepSPIM, PSNR=39.16dB. (h) Ground truth.

Table 2: The comparisons of PSNR values and SSIM values by different methods for sparse-view CT reconstruction on the test CT data set as shown in Fig. 3.

Views	Metrics	FBP	FNet	CSCGR	DFRP	WNet	DRONE	DeepSPIM
30 views	PSNR	26.03±0.51	34.98±0.97	35.60±0.81	35.63±0.99	38.97±0.78	38.02±0.70	**39.86±1.23**
	SSIM	0.458±0.025	0.880±0.010	0.914±0.005	0.895±0.010	0.947±0.009	0.934±0.028	**0.955±0.010**
45 views	PSNR	29.31±0.49	37.28±0.89	39.94±0.87	40.16±1.07	39.89±0.72	40.67±1.37	**43.00±0.84**
	SSIM	0.593±0.024	0.911±0.007	0.958±0.004	0.952±0.022	0.957±0.005	0.962±0.011	**0.973±0.004**
60 views	PSNR	31.68±0.49	39.45±0.88	42.52±0.82	43.70±1.02	43.43±0.65	42.72±0.84	**44.55±0.45**
	SSIM	0.693±0.023	0.931±0.012	0.974±0.004	0.975±0.023	0.975±0.003	0.976±0.046	**0.979±0.002**

3.3 Reconstruction results on large dataset

We validate the proposed method for sparse view reconstruction on the dataset "L067" from "NIH-AAPM-Mayo Clinic Low Dose CT Grand Challenge". The dataset includes 224 thoracic, abdominal, and pelvic images. These images are treated as ground truth.

We show an overall result of mean PSNR values and SSIM values, as well as the standard derivations in Table 3. The highest value is marked in **boldface**. It can be seen that the PSNR values and SSIM values by DeepSPIM are higher than other methods. Moreover, our PSNR and SSIM values outperform the second-best method by about 3dB and 0.01 on average, respectively. It shows the potential ability of DeepSPIM on large data sets.

Table 3: The comparisons of PSNR values and SSIM values by different methods for sparse-view CT reconstruction on the dataset "L067".

Images	Metrics	FBP	FNet	CSCGR	DFRP	WNet	DRONE	DeepSPIM
30 views	PSNR	25.71±0.50	32.83±0.88	34.53± 0.80	34.64±0.79	36.03±0.74	34.39±0.74	**39.33± 1.02**
	SSIM	0.496±0.027	0.722±0.016	0.901±0.012	0.900±0.021	0.925±0.007	0.896±0.012	**0.951±0.008**
45 views	PSNR	29.10±0.53	35.49±0.89	39.46±0.87	39.68± 1.02	39.45±0.63	39.56±1.31	**43.58±0.66**
	SSIM	0.641±0.026	0.649±0.016	0.953±0.006	0.949±0.013	0.955±0.005	0.955±0.057	**0.975±0.002**
60 views	PSNR	31.37±0.48	38.08±0.94	42.71±0.81	43.16±0.93	42.27±0.60	42.39±0.76	**45.13±0.58**
	SSIM	0.739±0.021	0.645±0.008	0.973±0.003	0.972±0.011	0.972±0.004	0.971±0.003	**0.981±0.002**

3.4 Noisy reconstruction results

We also test our method of reconstructing CT images from noisy projection data. The noisy projected data with 60 views is obtained by adding 1%, 2%, and 4% white Gaussian noise, respectively.

Fig. 6 shows the visual reconstructed results by different methods from 60 views and 4% Gaussian noises when reconstructing the image "08". It can be seen from Figs. 6(a)-6(b) that, FBP and FBPConvNet can not suppress the artifacts. The results by CSCGR and DFRP have noise residuals, see Figs. 6(c)-6(d). WNet provides an over-smoothed image, see Fig. 6(e). In Fig. 6(f), we can observe the obvious staircase artifacts. Compared with these methods, DeepSPIM can better reconstruct the image with more structures preserved and fewer artifacts residuals, see Fig. 6(g).

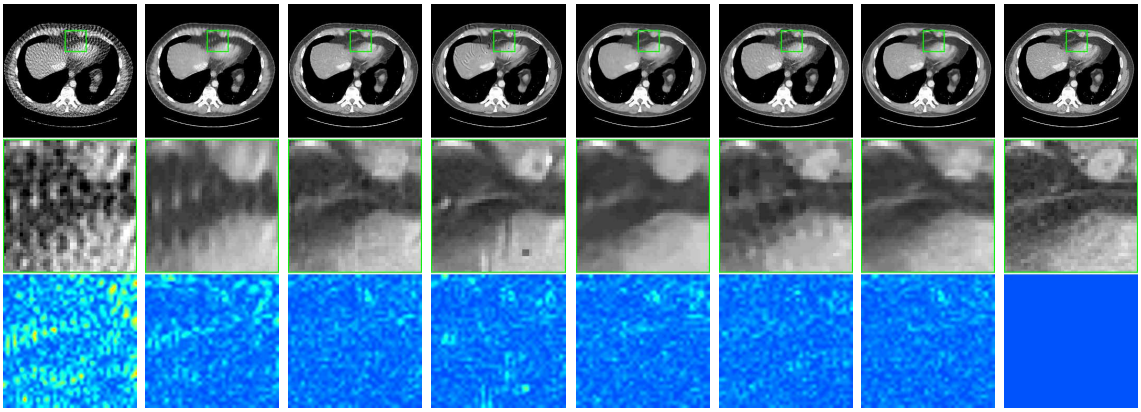

(a) FBP (b) FBPConvNet (c) CSCGR (d) DFRP (e) WNet (f) DRONE (g) DeepSPIM (h) Ground truth

Figure 6: Results of different methods when reconstructing the image "08" from 60 views with 4% Gaussian noise. The second row is the enlarged part in the first row. The third row is the difference between the reconstructed image u and the ground truth image I. (a) Result by FBP, PSNR=31.33 dB. (b) Result by FBPConvNet, PSNR=38.67dB. (c) Result by CSCGR, PSNR=41.05dB. (d) Result by DFRP, PSNR=41.21dB. (e) Result by WNet, PSNR=42.62 dB. (f) Result by DRONE, PSNR=42.31 dB. (g) Result by DeepSPIM, PSNR=43.49dB. (h) Ground truth.

The PSNR and SSIM values are reported in Table 4. It can be seen in Table 4 that, the performance for each method degrades when there is Gaussian noise in the projected data. However, DeepSPIM still outperforms the others by at least 1.05 dB in PSNR value and 0.051 in SSIM value on average. It validates the robustness of the proposed method under Gaussian noise.

Table 4: The comparisons of PSNR values and SSIM values by different methods for 60 views CT reconstruction with Gaussian noises on the test CT data set as shown in Fig. 3.

Views	Metrics	FBP	FNet	CSCGR	DFRP	WNet	DRONE	DeepSPIM
1%	PSNR	31.67±0.45	39.44±1.05	42.38±0.98	43.51±0.77	43.32±0.65	42.60±0.96	**44.51±0.49**
	SSIM	0.693±0.023	0.931±0.010	0.973±0.005	0.974±0.021	0.974±0.006	0.973±0.020	**0.979±0.005**
2%	PSNR	31.66±0.46	39.43±0.98	42.29±0.72	43.29±0.81	43.19±0.67	42.56±1.04	**44.35±0.53**
	SSIM	0.692±0.019	0.931±0.009	0.971±0.006	0.973±0.018	0.973±0.005	0.973±0.028	**0.978±0.004**
4%	PSNR	31.61±0.42	39.36±1.02	41.83±0.78	42.35±0.80	42.98±0.64	42.43±0.98	**43.77±0.55**
	SSIM	0.689±0.018	0.930±0.015	0.965±0.005	0.965±0.020	0.971±0.005	0.972±0.018	**0.976±0.006**

3.5 Ablation study

We train the DnCNN denoiser when the train set is replaced by 2174 CT medical images from the patients except for the patient "L067" from NIH-AAPM-Mayo Clinic Low Dose CT Grand Challenge. The proposed method with CT image trained DnCNN is referred to DeepSPIM-CT. Besides, we replace the denoiser DnCNN by multi-level wavelet convolutional neural network (MWCNN) [32], which has a UNet architecture. We train MWCNN with DIV2K dataset, and denote the method by DeepSPIM-MWCNN.

Tests are conducted on the dataset showed in Fig. 3. Quantitative results are reported in Table 5. It can be seen from Table 5 that when the denoiser is trained with CT images, the results are not satisfactory. Compared with CT images, DIV2K dataset contains many kind of natural images with different textures and structures, which helps the training of DnCNN. When the denoiser is MWCNN, the reconstruction results get better when there are 60 projection views. However, when the views are fewer, DeepSPIM with DnCNN denoiser provides a higher average PSNR and SSIM values.

Table 5: The comparisons of PSNR values and SSIM values by different methods for sparse-view CT reconstruction on the test CT data set as shown in Fig. 3.

Views	Metrics	DeepSPIM-CT	DeepSPIM-MWCNN	DeepSPIM
30 views	PSNR	37.44±1.00	39.53±0.94	**39.86±1.23**
	SSIM	0.931±0.011	0.940±0.006	**0.955±0.010**
45 views	PSNR	40.07±0.72	42.84±1.05	**43.00±0.84**
	SSIM	0.961±0.007	**0.974±0.007**	0.973±0.004
60 views	PSNR	41.37±0.72	**44.90±1.05**	44.55±0.45
	SSIM	0.968±0.010	**0.982±0.008**	0.979±0.002

3.6 Alternative methods

In Algorithm 1, we use the ADMM framework and add the semi-proximal term to the u-subproblem to make it solvable. An alternate algorithm for solving (2.1) is to use (2.2). We refer this algorithm to PnP-ADMM in [26] and solve it by adding a semi-proximal term to the v-subproblem, with $P=\alpha-\lambda R^{\mathrm{T}}R$. The iterations of PnP-ADMM becomes

$$\begin{aligned} u^{k+1} &= \arg\min_u F(u)+\frac{\beta}{2}\|u-v^k+b^k\|^2, \\ v^{k+1} &= \arg\min_v \frac{\lambda}{2}\|Rv-f\|^2+\frac{\beta}{2}\|u^{k+1}-v+b^k\|^2+\frac{1}{2}\|v-v^k\|_P^2 \\ &= \frac{\beta}{\alpha+\beta}(u^{k+1}+b^k)+\frac{\alpha}{\alpha+\beta}v^k-\frac{\lambda}{\alpha+\beta}R^{\mathrm{T}}(Rv^k-f), \\ b^{k+1} &= b^k+u^{k+1}-v^{k+1}. \end{aligned} \tag{3.2}$$

Another way to solve (2.1) is to add the semi-proximal term $\|u-u^k\|_P^2$ directly to (2.1) with $P=\alpha-\lambda R^{\mathrm{T}}R$, then solve

$$\begin{aligned} u^{k+1} &= \arg\min_u F(u)+\frac{\lambda}{2}\|f-Ru\|^2+\frac{1}{2}\|u-u^k\|_P^2 \\ &= \arg\min_u F(u)+\frac{\alpha}{2}\left\|u-u^k+\frac{\beta}{\alpha}R^{\mathrm{T}}(Ru^k-f)\right\|^2. \end{aligned} \tag{3.3}$$

We refer (3.3) to PnP-PGD in [36].

For DeepSPIM, PnP-ADMM, and PnP-PGD, we use the total variation image prior, or the deep prior by DnCNN, and fine tune the parameters to achieve the best reconstruction results.

In Fig. 7, we compare the proposed DeepSPIM, PnP-ADMM, and PnP-PGD when reconstructing the image "01" from 60 projection views. It can be seen from Figs. 7(b)-7(d) that, when it is TV prior, the results by DeepSPIM, PnP-ADMM and PnP-PGD are very similar. This is because that the three algorithms are guaranteed to converge to the minimizer of (2.1) when the prior is convex. However, when it is the deep prior, which may be potentially non-convex, the results by the three methods are very different, see Figs. 7(e)-7(g). The results by the proposed method has less residual, and a deep prior provides a better result than TV prior, see Figs. 7(d) and 7(g).

In Fig. 8, we compare the proposed DeepSPIM, PnP-ADMM, and PnP-PGD when reconstructing the image "02" from 30 projection views. Results in Figs. 8(b)-(d) are similar because of the convex TV prior. When it comes to the deep prior, the results are different, while DeepSPIM generates a satisfying image with clearer structures, see Figs. 8(e)-8(g).

Contrast to PGD, ADMM has been proven to converge to a stationary point even when the prior is non-convex, and restricted prox-regular, see [46]. Also in [36], in the experiments, PnP-ADMM has been shown to be more effective than PnP-PGD. Therefore, when F is a deep prior, DeepSPIM and PnP-ADMM work better than PnP-PGD. Compared with PnP-ADMM, DeepSPIM adds a semi-proximal term to the u-subproblem, and

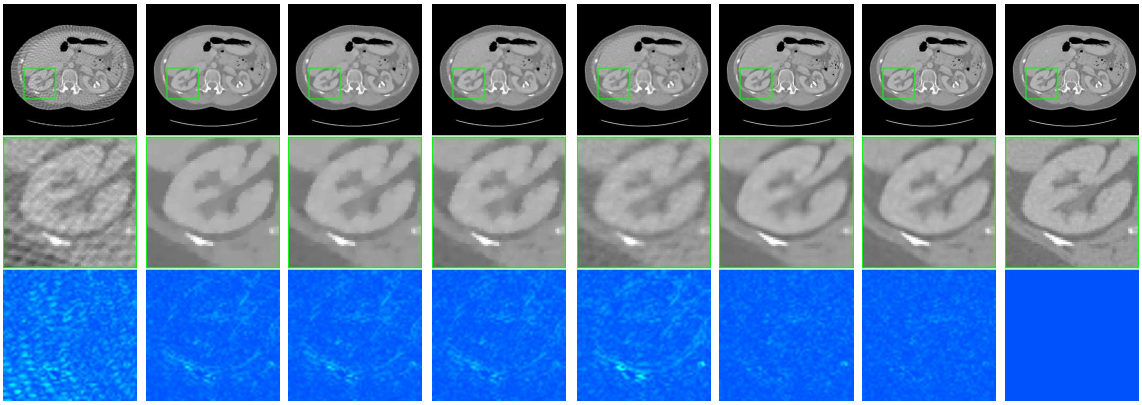

(a) FBP (b) PnP-PGD$_{TV}$ (c) PnP-ADMM$_{TV}$ (d) DeepSPIM$_{TV}$ (e) PnP-PGD$_{deep}$ (f) PnP-ADMM$_{deep}$ (g) DeepSPIM$_{deep}$ (h) Ground truth

Figure 7: Results by different methods when reconstructing the image "01" from 60 views. The second row is the enlarged part of the first row. The third row is the difference between the reconstructed image u and the ground truth image I. (a) Result by FBP, PSNR=32.12 dB. (b) Result by PnP-PGD with TV prior, PSNR=41.57dB. (c) Result by PnP-ADMM with TV prior, PSNR=41.63dB. (d) Result by DeepSPIM with TV prior, PSNR=41.64 dB. (e) Result by PnP-PGD with deep prior, PSNR=39.96 dB. (f) Result by PnP-ADMM with deep prior, PSNR=42.44 dB. (g) Result by DeepSPIM, PSNR=45.37 dB. (h) Ground truth.

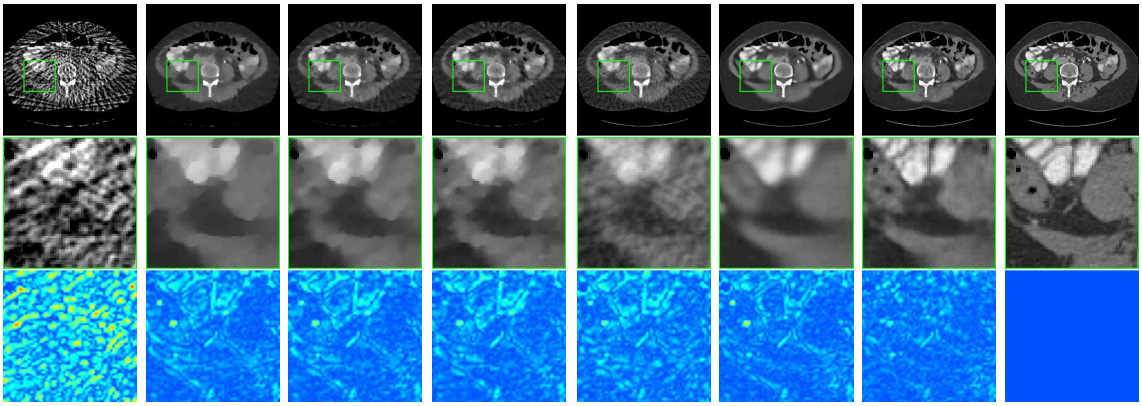

(a) FBP (b) PnP-PGD$_{TV}$ (c) PnP-ADMM$_{TV}$ (d) DeepSPIM$_{TV}$ (e) PnP-PGD$_{deep}$ (f) PnP-ADMM$_{deep}$ (g) DeepSPIM$_{deep}$ (h) Ground truth

Figure 8: Results by different methods when reconstructing the image "02" from 30 views. The second row is the enlarged part of the first row. The third row is the difference between the reconstructed image u and the ground truth image I. (a) Result by FBP, PSNR=25.40 dB. (b) Result by PnP-PGD with TV prior, PSNR=35.34dB. (c) Result by PnP-ADMM with TV prior, PSNR=35.40dB. (d) Result by DeepSPIM with TV prior, PSNR=35.40 dB. (e) Result by PnP-PGD with deep prior, PSNR=35.25 dB. (f) Result by PnP-ADMM with deep prior, PSNR=38.29 dB. (g) Result by DeepSPIM, PSNR=39.96 dB. (h) Ground truth.

makes it closer to a convex and proper subproblem than PnP-ADMM. Therefore, DeepSPIM approximates the global minimum better, and provides more satisfying results than PnP-ADMM. Overall, the experiments validate the effectiveness of DeepSPIM.

3.7 Computational time

To show the efficiency of the proposed method, we report the reconstruction time on CPU/GPU in seconds by different methods in Table 6. Compared with FBP, FBPConvNet, and WNet, DeepSPIM needs more time to get the final result. However, compared with other IR methods, the proposed method needs less time to reach a well-reconstructed image. A major reason is that the semi-proximal term in Algorithm 1 helps solve the u-subproblem, while in both CSCGR and DFRP, there is an inner loop to perform about 20 gradient descent-like steps in each outer iteration, and in DRONE, there is an inner loop with 100 steps for the total variation minimization.

We also plot the PSNR and SSIM curves when reconstructing the image "Abdominal" from 60 projection views by four IR methods (CSCGR, DFRP, DRONE, and ours) in Fig. 9. It can be seen that DeepSPIM needs less iterations (about 50 iterations) to converge, while CSCGR, DFRP, and DRONE need more than 100 iterations to converge. It also validates the global convergence result proved in Theorem 2.2.

Table 6: The comparisons of the reconstruction time in seconds by different methods for sparse-view CT reconstruction on the test CT data set as shown in Fig. 3.

Metrics	FBP	FNet	CSCGR	DFRP	WNet	DRONE	DeepSPIM
Time	**0.01 s**	3.7 s	811.8 s	976.2 s	6.4 s	40.1 s	10.8 s
Iteration	/	/	120	120	/	300	**50**

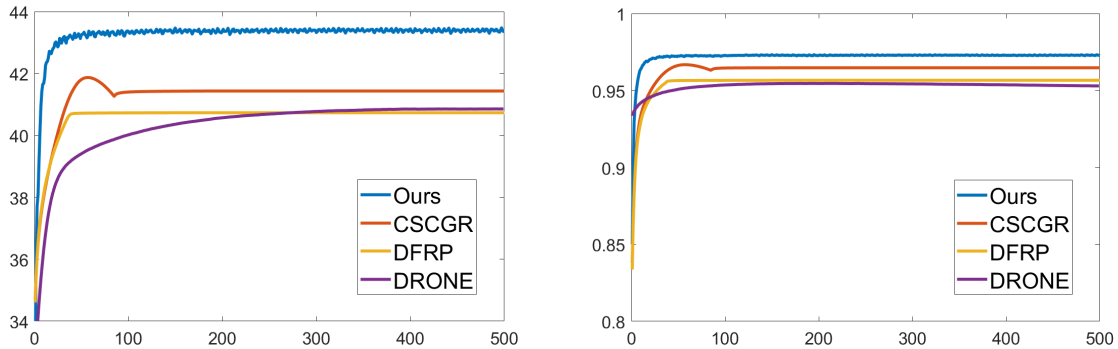

(a) PSNR curves (b) SSIM curves

Figure 9: PSNR and SSIM curves by CSCGR [3], DFRP [24], DRONE [47], and the proposed method DeepSPIM when reconstructing the CT image "Abdominal" with 60 projection views. x-axis: iteration number, y-axis: PSNR/SSIM value.

3.8 Parameter sensitivity

We test the influence of different parameters on the reconstruction results. Since in the experiments β is empirically set as $\beta = \alpha/\|R\|^2$, we only test λ when reconstructing the image "02" from 60 views and 4% Gaussian noise. In Fig. 10, we show the results. It can

be seen from Fig. 10 that the best PSNR and SSIM values can be attained by fine-tuning λ in the range [20,60]. When λ is too small, the penalty on the projection data is too weak, see the model (2.1). When λ is too large, the Gaussian noise cannot be removed effectively. Therefore, λ should be fine-tuned in experiments for different imaging settings. Overall, DeepSPIM is robust to λ in a large range.

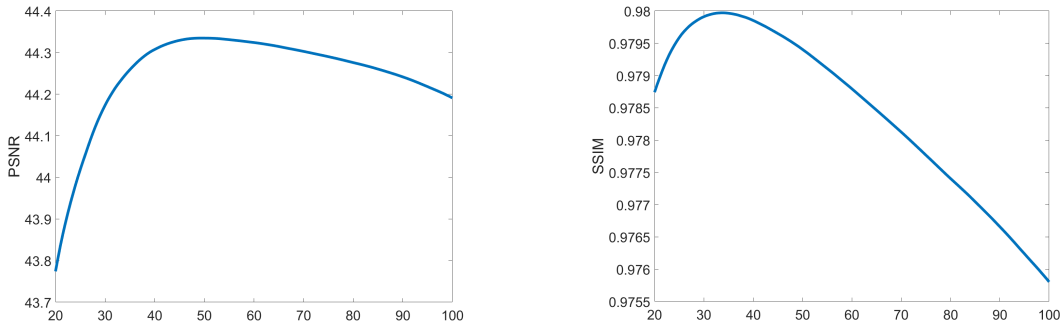

(a) PSNR curve (b) SSIM curve

Figure 10: PSNR and SSIM curves with different λ/β by DeepSPIM when reconstructing the image "02" with 60 projection views and 4% Gaussian noise. x-axis: λ/β, y-axis: PSNR/SSIM value.

4 Conclusion

In order to obtain high-quality reconstructed CT images, many model-based iterative reconstruction (IR) methods have been well studied. The model consists of a regularization prior term and a data fidelity term. Early IR methods focus on solving the model with a hand-crafted prior term by classical convex optimization algorithms. However, there are two core issues: it is difficult to solve the subproblem related to the system matrix; IR methods with hand-crafted priors can not provide satisfying reconstruction results.

For the first issue, since the system matrix has a large size, it is difficult to compute the Moore-Penrose Pseudo inverse. Instead, some works solve the subproblem by gradient-based methods, such as the separable paraboloid surrogate method, and conjugate gradient method. However, these gradient-based methods introduce an extra inner loop in each outer iteration, which increases the computational time and limits the further applications of IR methods.

For the second issue, many researchers try to incorporate iterative methods with a deep image prior in a plug-and-play fashion. However, it causes difficulty in the convergence proof. Instead, the convergence can only be verified empirically in experiments.

To address these issues, in this work, we propose DeepSPIM, an efficient semi-proximal iterative method with deep prior for sparse-view CT reconstruction. For the first issue, we aim to solve the subproblem in the proximal point strategy. A semi-proximal term is carefully designed to make the system matrix related subproblem solvable. As a result, without introducing extra inner iterations, this troubling subproblem can be

efficiently tackled. For the second issue, we use the residual-learning-based Gaussian denoiser DnCNN as the deep image prior. In order to establish the convergence of DeepSPIM, we assume that the network is a gradient step denoiser. By the derivations, we see that the gradient step denoiser outputs the difference between the input image and the predicted noise, which matches DnCNN. The existence of the solutions of the model over closed sets and the global convergence of DeepSPIM are established under reasonable assumptions.

Experiments show that DeepSPIM needs much less time to converge than other IR methods. Besides, compared with some state-of-the-art methods, DeepSPIM can better suppress the streaking artifacts when the projection views are sparse. Visual comparisons show that DeepSPIM can better preserve the fine details and structures in CT images. Reconstruction results on noisy projected data report the robustness of DeepSPIM. In future work, DeepSPIM can be improved by integrating a properly designed prior in the sinogram domain. The convergence result should also be established. In experiments, we find that DeepSPIM generates an over-smoothed result when it is Fanbeam geometry. We will extend the proposed method to more realistic projection geometry, such as Fanbeam geometry and Conebeam geometry.

In conclusion, the proposed method DeepSPIM has shown better reconstruction results than some state-of-the-art methods, including FBPConvNet, CSCGR, DFRP, WNet, and DRONE. It is emphasized that DeepSPIM is a global convergent iterative method with deep gradient step denoiser prior, which fills the gap in the IR methods for sparse-view CT reconstruction. DeepSPIM can be naturally extended to limited-angle CT [50], interior CT [53], positron emission tomography (PET) [33], and magnetic resonance imaging (MRI) [44].

Appendix A

A.1 Proof of Lemma 2.1

Proof. Obviously, P is symmetric. Note that $\|x\|_P = \sqrt{\langle x, Px\rangle}$. Since all the matrices and vectors discussed in this paper are real-valued, we have $\langle y, Px\rangle = \langle Px, y\rangle = \langle x, P^{\mathrm{T}}y\rangle$. For any $x \in \mathbb{R}^n$, we have

$$\begin{aligned}\langle x, Px\rangle &= \langle x, (\alpha I - \beta R^{\mathrm{T}}R)x\rangle = \alpha\langle x, x\rangle - \beta\langle x, R^{\mathrm{T}}Rx\rangle \\ &= \alpha\langle x, x\rangle - \beta\langle Rx, Rx\rangle = \alpha\|x\|^2 - \beta\|Rx\|^2 \\ &\geq (\alpha - \beta\|R\|^2)\|x\|^2 \geq 0. \end{aligned} \tag{A.1}$$

Therefore, P is positive semi-definite. We can then derive that

$$\begin{aligned}&\frac{\beta}{2}\|Ru - v^k + b^k\|^2 + \frac{1}{2}\|u - u^k\|_P^2 \\ =&\frac{\beta}{2}\langle Ru - v^k + b^k, Ru - v^k + b^k\rangle + \frac{1}{2}\langle u - u^k, P(u - u^k)\rangle\end{aligned}$$

$$
\begin{aligned}
&=\frac{\beta}{2}\langle Ru,Ru\rangle+\beta\langle Ru,b^k-v^k\rangle+\frac{\beta}{2}\langle b^k-v^k,b^k-v^k\rangle+\frac{\alpha}{2}\langle u-u^k,u-u^k\rangle\\
&\quad-\frac{\beta}{2}\langle u-u^k,R^{\mathrm{T}}R(u-u^k)\rangle\\
&=\frac{\beta}{2}\|Ru\|^2+\beta\langle u,R^{\mathrm{T}}(b^k-v^k)\rangle+\frac{\beta}{2}\|b^k-v^k\|^2+\frac{\alpha}{2}\|u\|^2-\alpha\langle u,u^k\rangle+\frac{\alpha}{2}\|u^k\|^2-\frac{\beta}{2}\|R(u-u^k)\|^2\\
&=\frac{\beta}{2}\|Ru\|^2+\beta\langle u,R^{\mathrm{T}}(b^k-v^k)\rangle+\frac{\beta}{2}\|b^k-v^k\|^2+\frac{\alpha}{2}\|u\|^2-\alpha\langle u,u^k\rangle+\frac{\alpha}{2}\|u^k\|^2-\frac{\beta}{2}\|Ru\|^2\\
&\quad+\beta\langle u,R^{\mathrm{T}}Ru^k\rangle-\frac{\beta}{2}\|Ru^k\|^2\\
&=\frac{\alpha}{2}\|u\|^2-\alpha\left\langle u,u^k-\frac{\beta}{\alpha}R^{\mathrm{T}}(Ru^k-v^k+b^k)\right\rangle+\frac{\beta}{2}\|b^k-v^k\|^2+\frac{\alpha}{2}\|u^k\|^2+\frac{\beta}{2}\|Ru^k\|^2\\
&=\frac{\alpha}{2}\left\|u-u^k+\frac{\beta}{\alpha}R^{\mathrm{T}}(Ru^k-v^k+b^k)\right\|^2-\frac{\alpha}{2}\left\|u^k-\frac{\beta}{\alpha}R^{\mathrm{T}}(Ru^k-v^k+b^k)\right\|^2\\
&\quad+\frac{\beta}{2}\|b^k-v^k\|^2+\frac{\alpha}{2}\|u^k\|^2+\frac{\beta}{2}\|Ru^k\|^2. \qquad \text{(A.2)}
\end{aligned}
$$

By omitting the constant terms with respect to u, we arrive at

$$
\begin{aligned}
&\arg\min_u F(u)+\frac{\beta}{2}\|Ru-v^k+b^k\|^2+\frac{1}{2}\|u-u^k\|_P^2\\
&=\arg\min_u F(u)+\frac{\alpha}{2}\left\|u-u^k+\frac{\beta}{\alpha}R^{\mathrm{T}}(Ru^k-v^k+b^k)\right\|^2, \qquad \text{(A.3)}
\end{aligned}
$$

which completes the proof. □

A.2 Proof of Theorem 2.1

Proof. To prove the theorem, we first show that the energy function $E(u)$ in (2.1) is proper and closed. Since Assumption 2.1 is satisfied, g_α is bounded from below. Therefore, F is also bounded from below by some constant C. It is obvious that E is proper because

$$E(u)=F(u)+\frac{\lambda}{2}\|Ru-f\|^2\geq C>-\infty. \qquad \text{(A.4)}$$

Besides, E is closed as a sum of closed functions.

If S is a compact set, then by the Weierstrass theorem for closed functions [4], we know E attains its minimal value over S, and the theorem is proved.

If R has full column rank, we show that E is coercive. Note that since R has full column rank, $R^{\mathrm{T}}R$ is positive definite. Thus, when $\|u\|\to+\infty$, $\|Ru\|\to+\infty$ and $\|Ru-f\|\to+\infty$. Therefore, we have

$$\lim_{\|u\|\to\infty}E(u)\geq\lim_{\|u\|\to\infty}C+\frac{\lambda}{2}\|Ru-f\|^2=+\infty. \qquad \text{(A.5)}$$

Thus, E is coercive with respect to u in $\mathbb{E}$.

Finally, we prove that E attains its minimal value over S. By the assumption $S\cap dom(F)\neq\emptyset$, we choose an arbitrary point $u_0\in S\cap dom(F)$. By the coerciveness of E, there exists an $A>0$ such that

$$E(u)>E(u_0) \tag{A.6}$$

for any $\|u\|^2>A$. Define $S_1=\{u\in\mathbb{E}:\|u\|^2\leq A\}$. Then, for any minimizer u^*, we have $E(u^*)\leq E(u_0)$, and that $u^*\in S_1\cap S$. $S_1\cap S$ is compact because it is the intersection of two bounded and closed sets. Therefore, by the Weierstrass theorem for closed functions [4], there exists at least one minimizer over S_1. Since $\emptyset\neq S_1\cap S\subset S$, there also exists at least one minimizer over S, which completes the proof. □

A.3 Proof of Theorem 2.2

Proof. The equality (2.9) holds under Assumption 2.1 according to [26]. Let

$$z^k=u^k-\frac{\beta}{\alpha}R^{\mathrm{T}}(Ru^k-v^k+b^k).$$

Since

$$u^{k+1}=Prox_{\frac{F}{\alpha}}(z^k)=\arg\min_u F(u)+\frac{\alpha}{2}\|u-z^k\|^2,$$

we have

$$F(u^{k+1})+\frac{\alpha}{2}\|u^{k+1}-z^k\|^2\leq F(u^k)+\frac{\alpha}{2}\|u^k-z^k\|^2, \tag{A.7}$$

$$F(u^{k+1})-F(u^k)\leq-\frac{\alpha}{2}\|u^{k+1}-u^k\|^2-\beta\langle u^{k+1}-u^k,R^{\mathrm{T}}(Ru^k-v^k+b^k)\rangle. \tag{A.8}$$

Therefore,

$$\begin{aligned}
&L_\beta(u^{k+1},v^k,b^k)-L_\beta(u^k,v^k,b^k)\\
=&F(u^{k+1})-F(u^k)+\frac{\beta}{2}\|Ru^{k+1}-Ru^k\|^2+\beta\langle Ru^{k+1}-Ru^k,b^k+Ru^k-v^k\rangle\\
\leq&-\frac{\alpha}{2}\|u^{k+1}-u^k\|^2-\beta\langle u^{k+1}-u^k,R^{\mathrm{T}}(Ru^k-v^k+b^k)\rangle\\
&+\frac{\beta}{2}\|Ru^{k+1}-Ru^k\|^2+\beta\langle Ru^{k+1}-Ru^k,b^k+Ru^k-v^k\rangle\\
\leq&\left(\frac{\beta}{2}\|R\|^2-\frac{\alpha}{2}\right)\|u^{k+1}-u^k\|^2.
\end{aligned} \tag{A.9}$$

The first "$\leq$" comes from (A.8). Besides, it can be easily seen that L_β is $(\lambda+\beta)$-strongly convex with respect to v. Thus,

$$L_\beta(u^{k+1},v^{k+1},b^k)-L_\beta(u^{k+1},v^k,b^k)\leq-(\lambda+\beta)\|v^{k+1}-v^k\|^2. \tag{A.10}$$

Note that the formula of v^{k+1} in (2.7) can be equivalently expressed as

$$\begin{aligned} v^{k+1} &= \frac{\lambda f+\beta R u^{k+1}+\beta b^k}{\lambda+\beta} = \frac{\lambda f+\beta v^{k+1}+\beta b^{k+1}}{\lambda+\beta}, \\ \lambda v^{k+1} &= \lambda f+\beta b^{k+1}, \\ b^{k+1} &= \frac{\lambda(v^{k+1}-f)}{\beta}. \end{aligned} \tag{A.11}$$

Thus, we obtain

$$\begin{aligned} &L_\beta(u^{k+1},v^{k+1},b^{k+1})-L_\beta(u^{k+1},v^{k+1},b^k) \\ =&\beta\langle b^{k+1}-b^k, Ru^{k+1}-v^{k+1}\rangle \\ =&\beta\|b^{k+1}-b^k\|^2=\frac{\lambda^2}{\beta}\|v^{k+1}-v^k\|^2. \end{aligned} \tag{A.12}$$

By putting (A.9), (A.10), and (A.12) together, we arrive at

$$\begin{aligned} &L_\beta(u^{k+1},v^{k+1},b^{k+1})-L_\beta(u^k,v^k,b^k) \\ \le&\left(\frac{\lambda^2}{\beta}-\lambda-\beta\right)\|v^{k+1}-v^k\|^2+\left(\frac{\beta}{2}\|R\|^2-\frac{\alpha}{2}\right)\|u^{k+1}-u^k\|^2. \end{aligned} \tag{A.13}$$

When $\lambda\le((1+\sqrt{5})/2)\beta$, and $\alpha\ge\beta\|R\|^2$, L_β is non-increasing.

By Assumption 2.1, g_α is bounded from below, hence L_β and F are also bounded from below.

On the feasible set Ω_f, $F(u)+(\lambda/2)\|f-v\|^2$ is coercive. Therefore, $\{(u^k,v^k)\}$ is bounded. Since $b^k=(\lambda/\beta)(v^k-f)$, $\{b^k\}$ is also bounded. By the non-increasing property of L_β, we have that $L_\beta(u^k,v^k,b^k)$ converges to the minimum $L_\beta(u^*,v^*,b^*)$ as k goes to infinity. In other words, (u^k,v^k,b^k) converges weakly to (u^*,v^*,b^*). □

A.4 Proof of Theorem 2.3

Proof. By the iteration of (2.7), we know $b^*=b^*+Ru^*-v^*$, and $v^*=Ru^*$. Thus,

$$L_\beta(u^*,v^*,b^*)=F(u^*)+\frac{\lambda}{2}\|f-Ru^*\|^2. \tag{A.14}$$

Now we prove that u^* is a minimizer of (2.1) by contradiction. Assume that u^* is not a minimizer of (2.1), that is, there exists a unique minimizer x, such that

$$F(x)+\frac{\lambda}{2}\|f-Rx\|^2<F(u^*)+\frac{\lambda}{2}\|f-Ru^*\|^2. \tag{A.15}$$

Let $y=Rx, z=0$. Then

$$L_\beta(x,y,z)=F(x)+\frac{\lambda}{2}\|f-Rx\|^2<F(u^*)+\frac{\lambda}{2}\|f-Ru^*\|^2=L_\beta(u^*,v^*,b^*), \tag{A.16}$$

which contradicts with the assumption that (u^*,v^*,b^*) is the unique minimizer of L_β. □

Acknowledgments

This work was supported in part by the Natural Science Foundation of Shanghai (Grant No. 22ZR1419500), by the Fundamental Research Funds for the Central Universities, Science and Technology Commission of Shanghai Municipality (Grant No. 22DZ2229014), and by the Natural Science Foundation of Chongqing, China (Grant No. CSTB2023NSCQ-MSX0276).

References

[1] E. Agustsson and R. Timofte, *NTIRE 2017 challenge on single image super-resolution: Dataset and study*, in: Proceedings of the IEEE Conference on Computer Vision and Pattern Recognition (CVPR) Workshops, 126–135, 2017.

[2] A. H. Andersen and A. C. Kak, *Simultaneous algebraic reconstruction techniques (SART): A superior implementation of the ART algorithm*, Ultrason. Imaging, 6(1):81–94, 1984.

[3] P. Bao et al., *Convolutional sparse coding for compressed sensing CT reconstruction*, IEEE Trans. Med. Imaging, 38(11):2607–2619, 2019.

[4] A. Beck, *First-Order Methods in Optimization*, in: MOS-SIAM Series on Optimization, SIAM, 2017.

[5] A. Beck and M. Teboulle, *A fast iterative shrinkage-thresholding algorithm for linear inverse problems*, SIAM J. Imaging Sci., 2(1):183–202, 2009.

[6] J. Bian, J. H. Siewerdsen, X. Han, E. Y. Sidky, J. L. Prince, C. A. Pelizzari, and X. Pan, *Evaluation of sparse-view reconstruction from flat-detector cone-beam CT*, Phys. Med. Biol., 55(22):6575–6599, 2010.

[7] S. Boyd, N. Parikh, E. Chu, B. Peleato, and J. Eckstein, *Distributed optimization and statistical learning via the alternating direction method of multipliers*, Found. Trends Mach. Learn., 3(1):1–122, 2011.

[8] D. J. Brenner, and E. J. Hall, *Computed tomography – an increasing source of radiation exposure*, N. Engl. J. Med., 375(22):2277–2284, 2007.

[9] S. H. Chan, X. Wang, and O. A. Elgendy, *Plug-and-play ADMM for image restoration: Fixed-point convergence and applications*, IEEE Trans. Comput. Imaging, 3(1):84–98, 2016.

[10] G.-H. Chen, J. Tang, and S. Leng, *Prior image constrained compressed sensing (PICCS): A method to accurately reconstruct dynamic CT images from highly undersampled projection data sets*, Med. Phys., 35(2):660–663, 2008.

[11] H. Chen, Y. Zhang, M. K. Kalra, F. Lin, Y. Chen, P. Liao, J. Zhou, and G. Wang, *Low-dose CT with a residual encoder-decoder convolutional neural network*, IEEE Trans. Med. Imaging, 36(12):2524–2535, 2017.

[12] P. Chen, J. Huang, and X. Zhang, *A primal–dual fixed point algorithm for convex separable minimization with applications to image restoration*, Inverse Problems, 29(2):025011, 2013.

[13] T. Cheslerean-Boghiu, F. C. Hofmann, M. Schultheiß, F. Pfeiffer, D. Pfeiffer, and T. Lasser, *WNet: A data-driven dual-domain denoising model for sparse-view computed tomography with a trainable reconstruction layer*, IEEE Trans. Comput. Imaging, 9:120–132, 2023.

[14] P. L. Combettes and V. R. Wajs, *Signal recovery by proximal forward-backward splitting*, Multiscale Model. Simul., 4(4):1168–1200, 2005.

[15] A. P. Dempster, N. M. Laird, and D. B. Rubin, *Maximum likelihood from incomplete data via the EM algorithm*, J. R. Stat. Soc., Ser. B, Methodol., 39(1):1–22, 1977.

[16] Q. Ding, G. Chen, X. Zhang, Q. Huang, H. Ji, and H. Gao, *Low-dose CT with deep learning regularization via proximal forward–backward splitting*, Phys. Med. Biol., 65(12):125009, 2020.
[17] B. Efron, *Tweedie's formula and selection bias*, J. Amer. Statist. Assoc., 106(496):1602–1614, 2011.
[18] I. A. Elbakri and J. A. Fessler, *Statistical image reconstruction for polyenergetic X-ray computed tomography*, IEEE Trans. Med. Imaging, 21(2):89–99, 2002.
[19] R. Gordon, R. Bender, and G. T. Herman, *Algebraic reconstruction techniques (ART) for three-dimensional electron microscopy and X-ray photography*, J. Theor. Biol., 29(3):471–481, 1970.
[20] H. Gupta, K. H. Jin, H. Q. Nguyen, M. T. McCann, and M. Unser, *CNN-based projected gradient descent for consistent CT image reconstruction*, IEEE Trans. Med. Imaging, 37(6):1440–1453, 2018.
[21] Y. Han and J. C. Ye, *Framing U-Net via deep convolutional framelets: Application to sparse-view CT*, IEEE Trans. Med. Imaging, 37(6):1418–1429, 2018.
[22] J. He, Y. Yang, Y. Wang, D. Zeng, Z. Bian, H. Zhang, J. Sun, Z. Xu, and J. Ma, *Optimizing a parameterized plug-and-play ADMM for iterative low-dose CT reconstruction*, IEEE Trans. Med. Imaging, 38(2):371–382, 2018.
[23] K. He, X. Zhang, S. Ren, and J. Sun, *Deep residual learning for image recognition*, in: IEEE Conference on Computer Vision and Pattern Recognition (CVPR), 770–778, 2016.
[24] Z. He, K. Hong, J. Zhou, D. Liang, Y. Wang, and Q. Liu, *Deep frequency-recurrent priors for inverse imaging reconstruction*, Signal Process., 190:108320, 2022.
[25] G. Huang, Z. Liu, L. Van Der Maaten, and K. Q. Weinberger, *Densely connected convolutional networks*, in: IEEE Conference on Computer Vision and Pattern Recognition (CVPR), 4700–4708, 2017.
[26] S. Hurault, A. Leclaire, and N. Papadakis, *Proximal denoiser for convergent plug-and-play optimization with nonconvex regularization*, in: Proceedings of the 39th International Conference on Machine Learning, PMLR, 162:9483–9505, 2022.
[27] K. H. Jin, M. T. McCann, E. Froustey, and M. A. Unser, *Deep convolutional neural network for inverse problems in imaging*, IEEE Trans. Med. Imaging, 26(9):4509–4522, 2017.
[28] A. C. Kak and M. Slaney, *Principles of Computerized Tomographic Imaging*, SIAM, 2001.
[29] E. Kang, J. Min, and J. C. Ye, *A deep convolutional neural network using directional wavelets for low-dose X-ray CT reconstrution*, Med. Phys., 44(10):e360–e375, 2017.
[30] S. Kawata and O. Nalcioglu, *Constrained iterative reconstruction by the conjugate gradient method*, IEEE Trans. Med. Imaging, 4(2):65–71, 1985.
[31] H. Kim, J. Chen, A. Wang, C. Chuang, M. Held, and J. Pouliot, *Non-local total-variation (NLTV) minimization combined with reweighted L1-norm for compressed sensing CT reconstruction*, Phys. Med. Biol., 61(18):6878, 2016.
[32] P. Liu, H. Zhang, W. Lian, and W. Zuo, *Multi-level wavelet convolutional neural networks*, IEEE Access, 7:74973–74985, 2019.
[33] G. Muehllehner and J. S. Karp, *Positron emission tomography*, Phys. Med. Biol., 51(13):R117–R137, 2006.
[34] R. T. Rockafellar, *Monotone operators and the proximal point algorithm*, SIAM J. Control Optim., 14(5):877–898, 1976.
[35] S. Ruder, *An overview of gradient descent optimization algorithms*, arXiv:1609.04747, 2016.
[36] E. Ryu, J. Liu, S. Wang, X. Chen, Z. Wang, and W. Yin, *Plug-and-play methods provably converge with properly trained denoisers*, in: Proceedings of the 36th International Conference on Machine Learning, PMLR, 97:5546–5557, 2019.
[37] C. Shen, Y. Lou, L. Chen, T. Zeng, M. K. Ng, L. Zhu, and X. Jia, *Comparison of three undersampling approaches in computed tomography reconstruction*, Quant. Imaging Med. Surg., 9(7):1229–

1241, 2019.
[38] R. L. Siddon, *Fast calculation of the exact radiological path for a three-dimensional CT array*, Med. Phys., 12(2):252–255, 1985.
[39] E. Y. Sidky, C.-M. Kao, and X. Pan, *Accurate image reconstruction from few-views and limited-angle data in divergent-beam CT*, J. Xray Sci. Technol., 14(2):119–139, 2006.
[40] E. Y. Sidky and X. Pan, *Image reconstruction in circular cone-beam computed tomography by constrained, total variation minimization*, Phys. Med. Biol., 53(17):4777, 2008.
[41] A. M. Teodoro, J. M. Bioucas-Dias, and M. A. Figueiredo, *A convergent image fusion algorithm using scene-adapted gaussian-mixture-based denoising*, IEEE Trans. Image Process., 28(1):451–463, 2019.
[42] *The 2016 NIH-AAPM-Mayo Clinic Low Dose CT Grand Challenge*, `http://www.aapm.org/GrandChallenge/LowDoseCT/`.
[43] S. V. Venkatakrishnan, C. A. Bouman, and B. Wohlberg, *Plug-and-play priors for model based reconstruction*, in: IEEE Global Conference on Signal and Information Processing, 945–948, 2013.
[44] M. T. Vlaardingerbroek and J. A. Boer, *Magnetic Resonance Imaging: Theory and Practice*, Springer, 2003.
[45] W. Wang, C. Wu, and Y. Gao, *A nonconvex truncated regularization and box-constrained model for CT reconstruction*, Inverse Probl. Imaging, 14(5):867–890, 2020.
[46] Y. Wang, W. Yin, and J. Zeng, *Global convergence of ADMM in nonconvex nonsmooth optimization*, J. Sci. Comput., 78:29–63, 2019.
[47] W. Wu, D. Hu, C. Niu, H. Yu, V. Vardhanabhuti, and G. Wang, *DRONE: Dual-domain residual-based optimization network for sparse-view CT reconstruction*, IEEE Trans. Med. Imaging, 40(11):3002–3014, 2021.
[48] W. Wu, Y. Zhang, Q. Wang, F. Liu, P. Chen, and H. Yu, *Low-dose spectral CT reconstruction using image gradient ℓ_0-norm and tensor dictionary*, Appl. Math. Model., 63:538–557, 2018.
[49] L. Xu, J. S. J. Ren, C. Liu, and J. Jia, *Deep convolutional neural network for image deconvolution*, in: Proceedings of the 27th International Conference on Neural Information Processing Systems, Vol. 1, 1790–1798, 2014.
[50] M. Xu, D. Hu, F. Luo, F. Liu, S. Wang, and W. Wu, *Limited-angle X-ray CT reconstruction using image gradient ℓ_0-norm with dictionary learning*, IEEE Trans. Radiat. Plasma Med. Sci., 5(1):78–87, 2021.
[51] Q. Xu, H. Yu, X. Mou, L. Zhang, J. Hsieh, and G. Wang, *Low-dose X-ray CT reconstruction via dictionary learning*, IEEE Trans. Med. Imaging, 31(9):1682–1697, 2012.
[52] X. Yang et al., *TV-based conjugate gradient method and discrete L-curve for few-view CT reconstruction of X-ray in vivo data*, Opt. Express, 23(5):5368–5387, 2015.
[53] H. Yu and G. Wang, *Compressed sensing based interior tomography*, Phys. Med. Biol., 54(9):2791, 2009.
[54] K. Zhang, W. Zuo, Y. Chen, D. Meng, and L. Zhang, *Beyond a Gaussian denoiser: Residual learning of deep CNN for image denoising*, IEEE Trans. Image Process., 26(7):3142–3155, 2017.
[55] H. Zhang, B. Liu, H. Yu, and B. Dong, *MetaInv-Net: Meta inversion network for sparse view CT image reconstruction*, IEEE Trans. Med. Imaging, 40(2):621–634, 2020.
[56] Z. Zhang, X. Liang, X. Dong, Y. Xie, and G. Cao, *A sparse-view CT reconstruction method based on combination of DenseNet and deconvolution*, IEEE Trans. Med. Imaging, 37(6):1407–1417, 2018.